

Highly Sensitive THz Refractive Index Sensor Based on Folded Split-Ring Metamaterial Graphene Resonators

Mohammad-Reza Nickpay

Semnan University

Mohammad Danaie (✉ danaie@semnan.ac.ir)

Semnan University <https://orcid.org/0000-0001-7046-2794>

Ali Shahzadi

Semnan University

Research Article

Keywords: Graphene, Absorber, Metamaterial, Surface Plasmons, Terahertz, Refractive Index Sensor

Posted Date: July 1st, 2021

DOI: <https://doi.org/10.21203/rs.3.rs-388749/v1>

License:  This work is licensed under a Creative Commons Attribution 4.0 International License.

[Read Full License](#)

Version of Record: A version of this preprint was published at *Plasmonics* on August 10th, 2021. See the published version at <https://doi.org/10.1007/s11468-021-01512-8>.

Highly Sensitive THz Refractive Index Sensor Based on Folded Split-Ring Metamaterial Graphene Resonators

Mohammad-Reza Nickpay, Mohammad Danaie*, Ali Shahzadi

Faculty of Electrical and Computer Engineering, Semnan University, Semnan, Iran

*: Corresponding author: danaie@semnan.ac.ir

Abstract- A highly sensitive absorption-based sensor based on folded split-ring metamaterial graphene resonators (FSRMGRs) is designed, and its biomedical application in terahertz (THz) spectrum is investigated. The sensor has a nearly perfect absorption with a spectral absorption coefficient of 99.75% at 4 THz, with a high *Q*-factor (average) of 13.76. The resonance peak frequency is sensitive to the refractive index (RI) of the test medium (analyte) and a fairly high sensitivity of 851 GHz/RIU has been obtained. The specifications of the sensor can be tuned by an external DC-bias voltage applied to the graphene layer. According to the obtained results, the developed absorber appears to be a good candidate bio-sensing applications.

Keywords: Graphene, Absorber, Metamaterial, Surface Plasmons, Terahertz, Refractive Index Sensor.

1. Introduction

The terahertz (THz) electromagnetic spectrum (0.3–10 THz) has attracted significant interest due to the unique features of its frequency band. One of the most frequently used THz applications are electromagnetic wave absorbers [1]. The absorbing structures can be used to design biomedical devices and sensors [2-7]. Meanwhile, metamaterials (MTMs) are artificial electromagnetic metal nanostructures originating from periodic single-cell arrays that are considerably smaller in size than the operational wavelength [8]. Because of the unique attributes of MTMs, which are not available in natural materials such as negative refractive index (RI) [9-12], MTMs are used to design and fabricate metamaterial perfect absorbers (MPA). Some applications of the MPA are in sensing [13], [14], photo-thermal conversion, micro-bolometers, photo-catalysis, and thermal emitters [15–22].

MPA can be used as a RI sensor with a high sensitivity to changes in the characteristics of its environment [23-27]. The RI sensors based on the structure of the MTMs can have a high detection speed and low environmental damages, and they are excellent options for biomedical sensing [28–32]. As some examples, a biosensor with combined resonators on a silicon substrate with a sensitivity of 85 GHz/RIU is represented in [33]. A refractive index MTMs biosensor based on split-ring resonator (SRR) on a Teflon substrate with a sensitivity of 300 GHz/RIU is represented in [34]. Finally, a high-sensitivity MTMs biosensor based on double-ring shaped reported in [35] has a sensitivity of 638 GHz/RIU.

Graphene is a two-dimensional (2D) single-layer structure in which carbon atoms are coordinated into a honeycomb structure. In the far-infrared to THz band, graphene supports surface plasmonic polaritons (SPPs) [36-42] and they have strong electric field constraints and low loss optical attributes compared to other plasmonic metals such as gold and silver [43], [44]. Also, graphene plasmonic sensors can improve sensing characteristics due to the high amount of modal confinement in graphene-insulator surfaces [45]. Compared to conventional materials, we can change its surface conductivity by using an external DC-bias voltage. The graphene conductivity regulation is due to a change in the Fermi level where it can be used to change the resonance peak frequency of an absorber in a wide spectrum [28].

In this paper, we have proposed a high sensitivity RI sensor composed of an array of folded split ring MTMs graphene-based resonators (FSRMGRs). Having an absorption value of 98.7% and a Q-factor of 13.76 for the resonance frequency, the proposed sensor provides a good frequency selectivity. Besides, the sensor has a high sensitivity of 851 nm/RIU (where RIU stands for refractive index unit) to changes in its environment, which can be a biological tissue under test with different refractive indices. The outcome of the work indicates that the designed structure can be used for THz biomedical sensors applications.

2. Graphene Conductivity

Graphene's surface conductivity is expressed as a function of σ_g (ω , μ_c , τ , T). The conductivity calculations were investigated using the Kubo formula [46]. In the function of σ_g , ω is the angular frequency, μ_c is chemical potential, $2\Gamma = \tau^{-1}$, whereas $\tau = \mu_m \mu / e v_f^2$ is the electron relaxation time in graphene where μ_m is the carrier mobility and $v_f = 10^6 \frac{m}{s}$ is the Fermi velocity. T is temperature and in terms of Kelvin. The characteristics of graphene-based devices, such as the absorbers and sensors, can be changed using the argument variables in σ_g .

The graphene conductivity consists of a collection of two inter-band and intra-band terms. [36]. The surface conductivity of graphene is described as Eq. (1):

$$\sigma_g(\omega, \mu_c, \Gamma, T) = \sigma_{\text{intra}} + \sigma_{\text{inter}} \quad (1)$$

Where:

$$\sigma_{\text{intra}} = \frac{i q_e^2 K_B T}{\pi(\omega + i 2\Gamma) \hbar^2} \left(\frac{\mu_c}{K_B T} + 2 \ln \left(e^{-\mu_c/(K_B T)} + 1 \right) \right) \quad (2)$$

$$\sigma_{\text{inter}} = \frac{i q_e^2}{4\pi\hbar} \ln \left[\frac{2|\mu_c| - (\omega + i 2\Gamma)\hbar}{2|\mu_c| + (\omega + i 2\Gamma)\hbar} \right] \quad (3)$$

Here, $q_e = 1.6 \times 10^{-19}$ C is the charge of the electron, \hbar is the reduced Plank's constants, and K_B is the Boltzmann's constant. The chemical doping and electrical gating are two primary methods of adjusting the Fermi level of graphene. The form of electrical gating by using external DC-bias voltage is shown in Fig. 1. The voltage V_G is used to adjust the chemical potential (μ_c) of the graphene layer (See Eq. (4)) and consequently, the Fermi level.

$$V_G = V_0 + \frac{H_t q_e \mu_c^2}{\varepsilon_0 \varepsilon_r \pi \hbar^2 v_f^2} \quad (4)$$

Where, V_0 is the voltage compensation related to the chemical doping, H_t and ε_r are the thickness and relative permittivity of the dielectric between graphene and electrode, respectively, and $v_F = 9.5 \times 10^5$ m/s is the Fermi velocity [36].

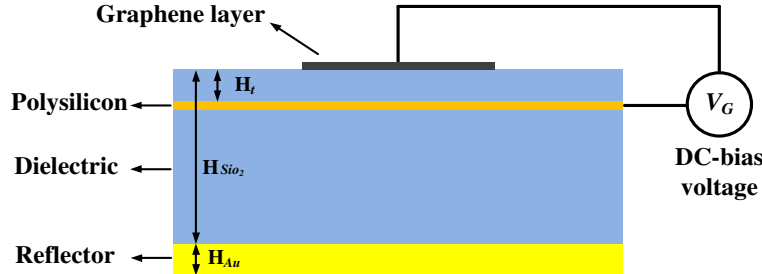


Fig. 1. Arrangement of the proposed structure and applying the external gate voltage V_G .

The gate bias is applied between the graphene layer and polysilicon DC gating pads, separated by a thin layer of SiO_2 . The thickness of the polysilicon layer is negligible and does not affect the overall performance of the designed structure. Implying $V_0=0$, $\varepsilon_r = 3.9$, the variation of the chemical potential (μ_c) for the different values of the external DC-bias voltage (V_G) is shown in Fig. 2. Also, Fig. 2 indicates the change in chemical potential (μ_c) for different substrate thickness (H_t) values. It is evident that lower values of H_t are needed to achieve a higher value of μ_c at a specific voltage.

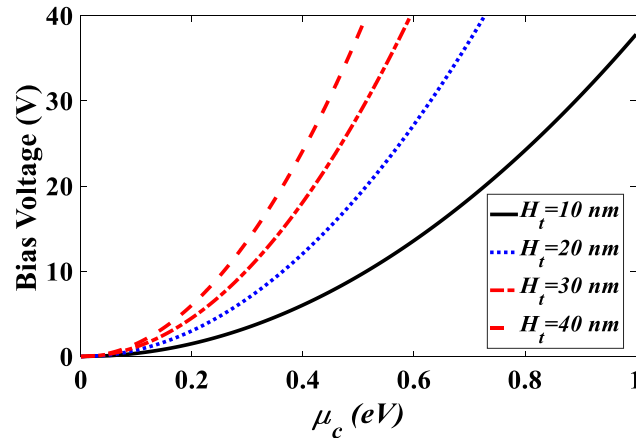


Fig. 2. Variation in the chemical potential μ_c for the different values of the external V_g and for the different thickness values of the substrate.

3. Structure design and numerical model

The proposed FSRMGRs is shown in Fig. 3. The perspective view of the unit cell of the designed structure is shown in Fig. 3(a), which consists of three layers of the metallic plate, dielectric, and resonators. The metallic plate is a gold layer and acts as a reflector. Gold is a lossy metal, and its electrical conductivity is $\sigma = 4.56 \times 10^7 S/m$. The dielectric layer is silica (SiO_2) with electric permittivity $\varepsilon_r = 3.9$ and has a $4.625 \mu m$ thickness. Fig. 3(b) shows the front view of the top layer consists of a $0.35 nm$ thick FSRMGRs array with corresponding the

geometric parameters are $H_{Au} = 0.2 \mu m$, $H_{SiO_2} = 4.625 \mu m$, $R_{out} = 2 \mu m$, $R_{in} = 1.45 \mu m$, $W_1 = 1 \mu m$, $W_2 = 0.45 \mu m$, $W_3 = 0.25 \mu m$, $W_4 = 0.35 \mu m$, $W_5 = 0.45 \mu m$, respectively. The proposed structure's period is $L = 4.75 \mu m$.

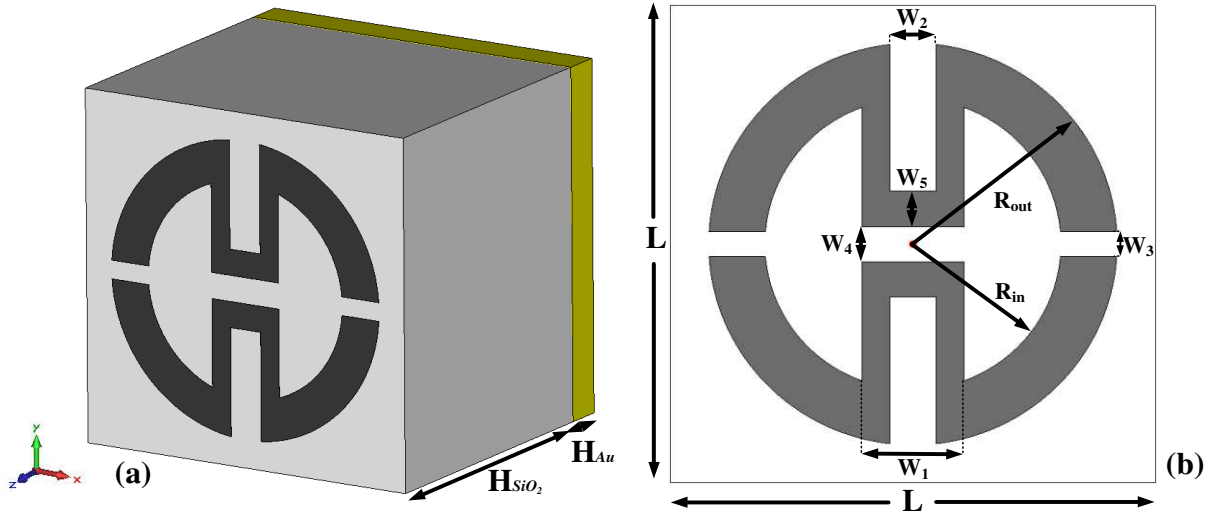


Fig. 3. (a) The perspective view of the proposed THz structure consisting of graphene and reflector gold film, separated by a SiO_2 spacer. (b) front view of the top layer of the proposed graphene array.

Due to the thickness of the gold plate, and the fact that wave does not pass through it, the absorber's transmission coefficient is zero ($T(\omega) = |S_{21}|^2 = 0$). The absorption coefficient of the structure is defined as $A(\omega) = 1 - R(\omega) - T(\omega)$, where $R(\omega)$ is the reflection coefficient and all three coefficients are functions of frequency. As a result, the absorption coefficient of the proposed THz absorber is equal to $A(\omega) = 1 - R(\omega) = 1 - |S_{11}|^2$ [1].

The reflection coefficient can become zero if the appropriate parameters are chosen for the graphene layer so as to ensure that the impedance at the top of the structure matches well to 120π ohm impedance of free space. The dielectric layer in the designed structure acts like a Fabry–Perot cavity due to the existence of the graphene resonators and the metallic reflective plate. Note that graphene has a metallic behavior at the THz spectrum and traps the incident wave inside the structure [47].

To ensure high-performance single-band MPA for sensing applications, the unit cell specifications must be expertly optimized. The proposed absorber was numerically simulated using the CST Microwave Studio software. When setting boundary conditions, the x/y-directions of the unit cell are chosen as periodic, and a z-direction open boundary is used. The incident wave was represented as a Floquet port in the z-direction (with an electric component along the y-direction). The proposed system is simulated using hexahedral meshes. Finally, the frequency-domain solver is used to analyze the designed structure. The results will be presented in Section 4.

4. Results and discussion

The absorption spectrum of the optimized structure for specific graphene layer parameters, including, $\mu_c = 0.5 \text{ eV}$, $\tau = 1 \text{ ps}$, and $T=300^\circ\text{K}$ is shown in Fig. 4, a perfect narrow-band absorption peak at 4 THz is achieved.

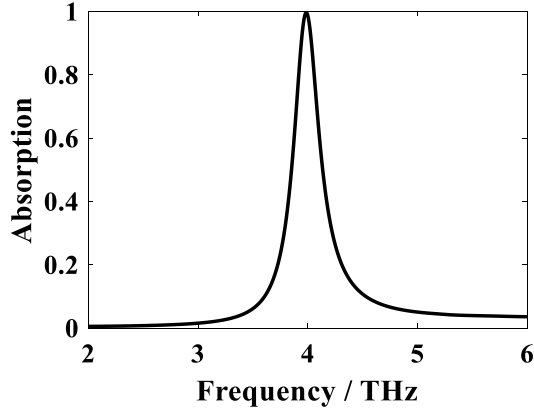


Fig. 4. The absorption spectrum of the proposed structure.

The distribution of the absolute value of the electric field for the proposed THz structure at the resonance frequency of 4 THz is presented in Fig. 5(a). As seen in Fig. 5(a), when $f= 4 \text{ THz}$, the electric field is almost balanced on the FSRMGRs and concentrated near the gaps of the resonance. Fig. 5(b) shows the electric field at 5.56 THz (out of resonance), which it is clear that at this frequency, there is almost no electric field distribution in FSRMGRs. According to Eq. (1-3), when the chemical potential μ_c increases, graphene's surface conductivity increases. The absorption spectrum for different values of μ_c is shown in Fig. 6. As seen when the chemical potential increases to $\mu_c = 0.5 \text{ eV}$, the absorption value of the graphene-based structure increases and then decreases. Furthermore, as the μ_c increases, the resonance frequency of the proposed MPA is blue-shifted, and the absorption peak frequency changes from 1.86 THz to 5.2 THz. It is worth mentioning that in this work, the chemical potential of graphene is in the range of 0.1–0.9 eV, which can be calculated using Eq. (4) and generated from an external DC source with the range of 13.6–30.6 V.

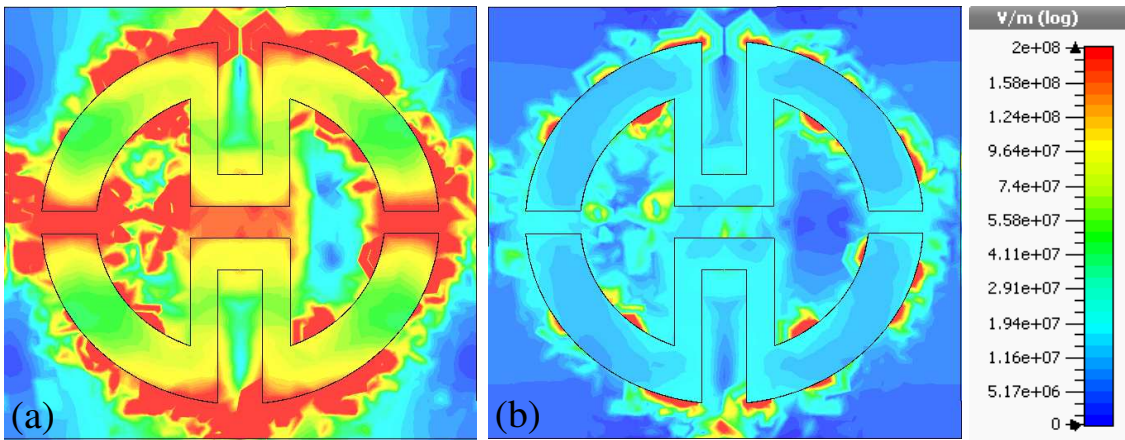


Fig. 5. Electric field (Abs) distribution of the proposed THz structure at (a) 4 THz, (b) 5.56 THz.

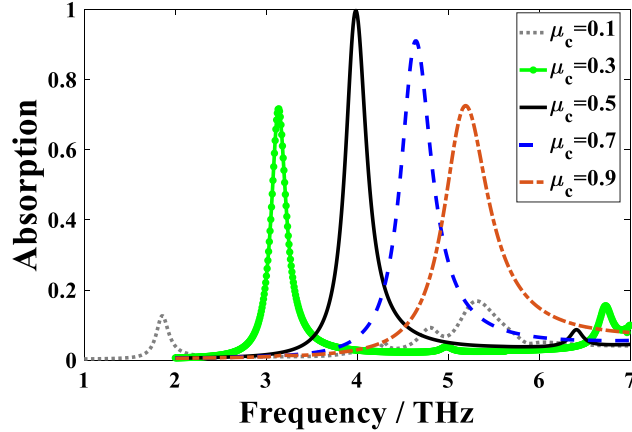


Fig. 6. The absorption spectrum for different values of μ_c .

The Equivalent circuit model of the MPA is shown in Fig. 7. The resonance frequency of the MPA expressed as:

$$f = 1/2\pi\sqrt{L_{eq}C_{eq}} \quad (5)$$

Where, L_{eq} and C_{eq} are the equivalent capacitance and inductance, respectively [2], [48]. The increase in μ_c will result in a decrease in L_{eq} due to the absorption peak's shifting to higher frequencies. The concentration of the carrier will increase as the chemical potential μ_c increases from 0.1 eV to 0.5 eV, leading to increased excitation of the SPPs [49], [50]. Therefore, the absorption value rises. When the μ_c reaches 0.5 eV and relaxation time $\tau=1$ ps, the SPPs resonance reaches a maximum. As a result, by applying a DC-bias voltage, we can both precisely adjust our desired resonance frequency of the graphene-based devices, which is useful for systems that need to be recalibrated. Also, we can significantly improve the performance of the designed system. Here the goal is to increase the value of absorption at the resonance frequency.

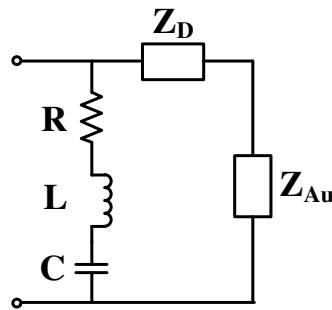


Fig. 7. The equivalent circuit model of the MPA.

At this point, the influences of the geometric parameters such as R_{in} , W_1 , W_2 , and W_3 on the function of the single-band MPA are studied. Given that our proposed structure is also essentially a ring, the results of previous work on the ring structure can be used. The inductance of the simple ring is related to the approximated formula [51]:

$$L_{eq} \sim \frac{\mu_0 \pi R_m^2}{H_{graphene}} \quad (6)$$

Where, μ_0 is the free-space permeability and $R_m = (R_{in} + R_{out})/2$.

Increasing the internal radius (R_{in}) of the FSRMGRs decreases the width of the graphene strip, resulting in a higher inductance value, which causes a red-shift in the resonance frequency. It is in good agreement with the absorption spectrum shown for the different R_{in} in Fig. 8. In the meantime, by increasing R_{in} , the absorption peak frequency and the Q -factor value decrease.

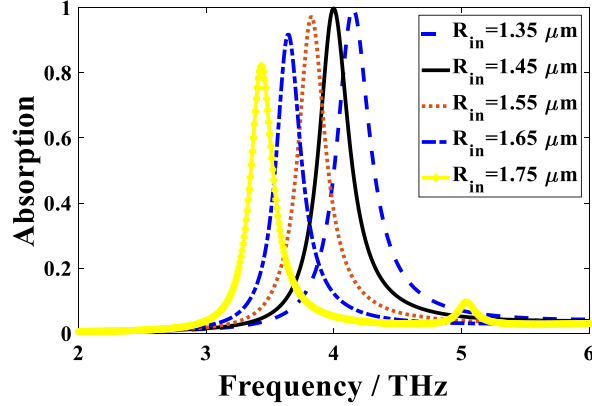


Fig. 8. The absorption spectrum of the proposed structure when R_{in} changes.

Increasing W_1 will induce a lower inductance value. Although the capacitance increases consequently, the influence of the inductance in the resonance frequency is more relevant, resulting the resonance frequency to have a blue-shift. This trend is shown in Fig. 9. In the meantime, the absorption peak frequency and the Q -factor value increase.

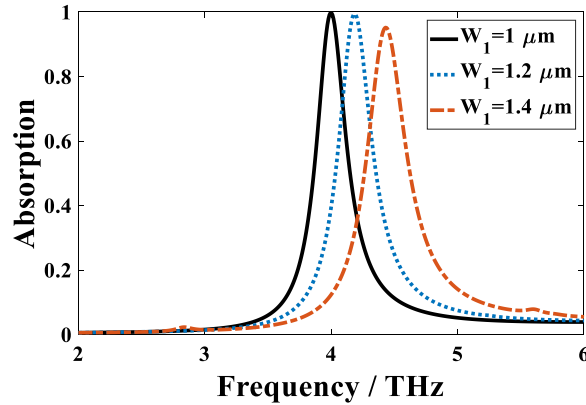


Fig. 9. The absorption spectrum of the proposed structure when W_1 changes.

Increasing the width of the FSRMGRs (W_2) will decrease the width of the graphene strip, resulting in a higher inductance value, which causes the resonance frequency to have a red-shift. This trend is shown in Fig. 10. In the meantime, the absorption peak frequency and the value of the Q -factor increase to $W_2 = 0.45 \mu m$ and then decrease.

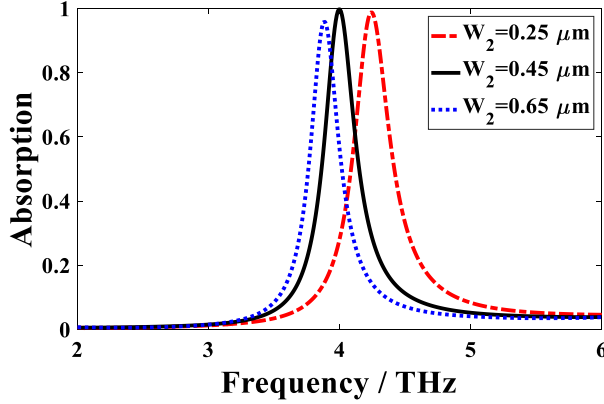


Fig. 10. The absorption spectra of the proposed structure when W_2 changes.

The gap between two split rings W_3 can be considered as a parallel plate capacitor. Thus its capacitance is related to [51]:

$$C_{eq} \sim \epsilon_0 \frac{H_{graphene} \times (R_{out} - R_{in})}{W_3} \quad (7)$$

Where, ϵ_0 is the free-space permittivity. Therefore, the wider the gap between the two rings, the smaller the corresponding capacitance. Moreover, the inductance decreases as the amount of graphene strip decrease as a result of increasing W_3 . Fig.11 shows the absorption spectrum for different values of W_3 between $0.25 \mu m$ and $0.75 \mu m$, which introduces the resonance frequency with a blue-shift.

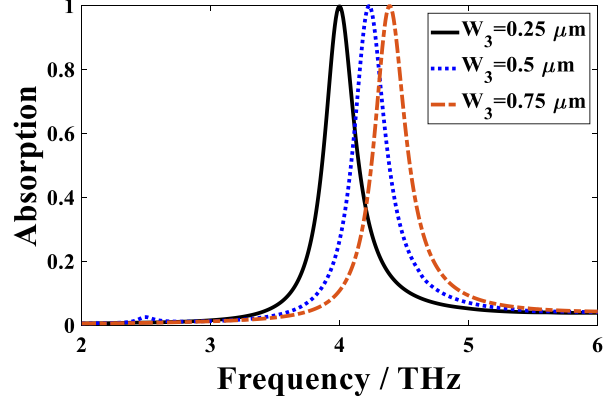


Fig. 11. The absorption spectrum of the proposed structure when W_3 changes.

When the absorber is designed to be used as a sensor, its equivalent capacitance, in addition to its dependence on the dielectric material between the graphene layer and the reflector, also depends on the RI and thickness of the analyte. Changing the RI and thickness of the analyte changes the value of the equivalent capacitance, thus changing the absorption peak frequency, which is the same as the sensor application of the designed structure. The designed plasmonic RI sensor based on a graphene-based MTM absorber is shown in Fig. 12, in which a test medium (analyte) with the thickness of $H_{Analyte} = 1 \mu m$ is placed at the top of the structure. The equivalent circuit model of the FSRMGRs sensor is shown in Fig. 13. The resonance frequency of the sensor expressed as:

$$f = \frac{1}{2\pi\sqrt{L_{eq}(C_{eq} + C_{Analyte})}} \quad (8)$$

Since C_{eq} has a small value versus $C_{Analyte}$, the equivalent capacitance of the sensor is more affected by the analyte parameters. As a result, a slight change in the analyte characteristics, including thickness and RI, can cause significant changes in the absorption frequency and absorption value, making it suitable for use in sensor applications.

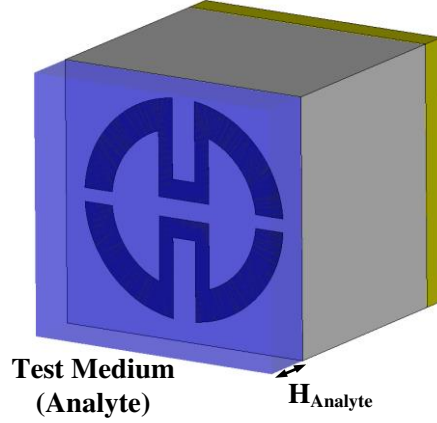


Fig. 12. The proposed plasmonic RI sensor based on a graphene-based MTM absorber.

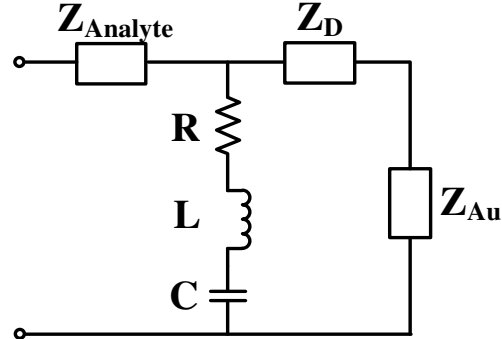


Fig. 13. The Equivalent circuit model of the sensor.

The sensing application is one of the fields in which the MPA can be used [52]. This technique is based on changes in the surrounding medium's RI which changes the metamaterial plasmonic structure's resonance frequency. The sensitivity (S), FOM, and Q -factor are the three critical parameters for measuring and ensuring the performance of a sensor [53], [54]:

$$S = \frac{\Delta f}{\Delta n} \quad (9)$$

$$FOM = \frac{S}{FWHM} \quad (10)$$

$$Q = \frac{f}{FWHM} \quad (11)$$

Here, Δf is the frequency change of the absorption peak, Δn is the RI change, and FWHM represents the full width at half maximum [4]. Fig. 14 shows the absorption spectrum while the

RI of the surrounding medium (analyte) is changed from 1.0 to 1.6 (with a thickness $H_{\text{Analyte}} = 1 \mu\text{m}$). The resonance peak frequency has a red-shift when the RI rises. Due to fact that the dielectric constant ϵ_r is proportional to the RI (n) with $\epsilon_r = n^2$ [55], increasing the RI causes the capacitance of the analyte layer (C_{Analyte}) to increase. As a result, according to Eq. (5), the resonance peak frequency has a red-shift when the RI rises. It should be noted that the RI of the normal biomedical analyte is generally in the range of 1.3 - 1.5. For example, the blood refractive index for healthy human beings is 1.35, and the n of blood samples infected with subtypes of avian influenza viruses are almost 1.5. Also, the refractive index of blood for Human MCF-7 breast cancer is 1.401 [56] and for blood samples infected with T-type leukemia is 1.39.

For the biosensor evaluation, we used the RI of the analyte in the range of 1.35–1.4 when n changing with a step of 0.01. The variation of the absorption peak frequency is significant even though the n changes are tiny. As shown in Fig.14, the proposed sensor can be used for highly sensitive biosensor applications.

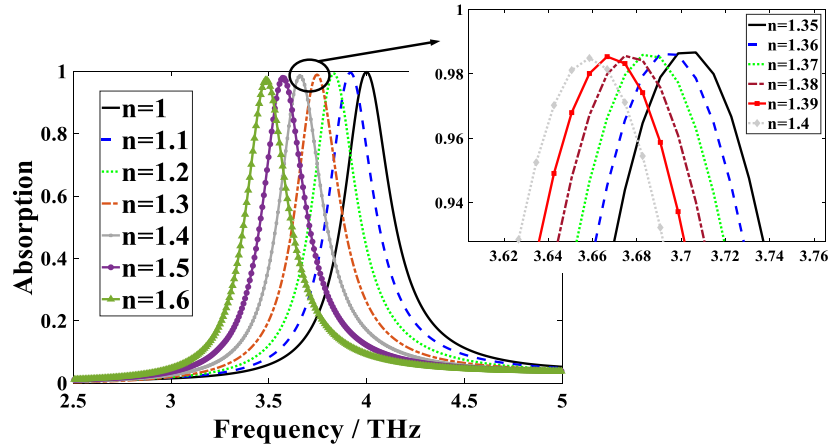


Fig. 14. Absorption spectra vs. the changes of the RI of the analyte.

The sensitivities of the proposed plasmonic graphene-based sensor are presented in Table (1) for each RI values. Based on the results provided in Table. 1, the maximum sensitivity is 860 GHz/RIU which is a significant result compared to current research [57-67]. According to the formula $|d\lambda/dn| = c/f_0^2 \times (df/dn)$ [67], where c is the speed of light, f_0 is the resonance frequency, and n represents the refractive index of the analyte, the maximum sensitivity is corresponds to $16.125 \mu\text{m}/\text{RIU}$. Another sensor parameter is the figure of merit (FoM). The values of the FoM for each RI are also represented in Table (1). According to the results of sensitivities and the FoM presented in Table. 1 and as well as comparisons with similar research, the proposed sensor is very suitable for medical applications such as sensing, cancer cells, and virus detection. In summary, the average FWHW of the resonance peak frequency is 272 GHz . According to Eq. (9), (10) and (11), the average sensitivity $S = 851 (\text{GHz}/\text{RIU})$ (corresponding to $15.59 \mu\text{m}/\text{RIU}$), $\text{FoM} = 3.16 (1/\text{RIU})$ and Q -factor of 13.76 for resonance peak frequency.

Table 1. The resonance peak frequency (RPF), the shift of RPF (ShRPF), sensitivity (S), The FWHM, FoM, and Q -factor using different RI of test medium (analyte).

Refractive index	RPF	ShRPF [THz]	S [THz/RIU]	FWHM [THz]	FoM	Q -factor
1	4	----	----	0.286	----	13.98
1.1	3.914	0.086	0.860	0.282	3.04	13.87
1.2	3.834	0.166	0.830	0.278	2.98	13.79
1.3	3.746	0.254	0.846	0.272	3.11	13.77
1.4	3.658	0.342	0.855	0.267	3.2	13.7
1.5	3.570	0.430	0.860	0.261	3.29	13.67
1.6	3.486	0.514	0.856	0.257	3.33	13.56

As shown in Fig. 15, resonance peak frequency changes have a linear performance in terms of analyte RI changes.

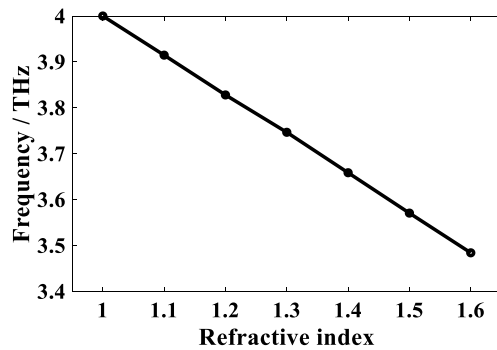


Fig. 15. The resonance peak frequency changes with the analyte RI changes.

The effect of the refractive index changing on the maximum absorption of the sensor is shown in Fig. 16. There is a very slight decrease in the overall absorption of the proposed sensor relative to the rise in the refractive index, which is beneficial.

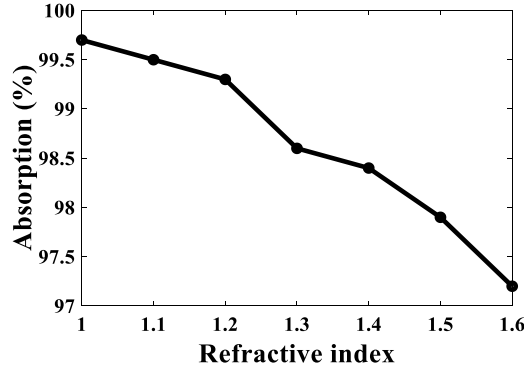


Fig 16. The effect of the refractive index changing on the maximum absorption of the sensor.

Table (2) compares the results obtained in this paper with the most recent works in the literature. As seen the proposed method provides the highest sensitivity among the similar works reported in the literature.

Table 2. Comparison of the sensing performance of the proposed sensor with the previous works.

Reference	Year	Topology	Operating Range [THz]	Sensitivity [GHz/RIU]
[57]	2009	Parallel-plate waveguide resonance cavity	0.1-0.5	91.25
[58]	2012	Parallel-plate waveguide resonance cavities	0.2-0.3	225
[59]	2013	Hybrid terahertz plasmonic waveguide	0-1.2	261
[60]	2014	Metamaterial absorbers	0.5-1	163
[61]	2014	Photonic column array	0.4-3	261
[62]	2016	Metal-dielectric-metal waveguide	0-3	457
[63]	2016	Dielectric sensor	0.5-1	500
[64]	2019	Metamaterial reflector	0-3	540
[65]	2018	Double ring sensor	3.82	160
[66]	2013	Fourfold symmetric metamaterials	2-5.5	130
[67]	2018	Graphene micro-ribbon array	1.5-6.5	360
[33]	2019	H-shaped Resonator	0.6-1.2	85
[34]	2019	Plasmonic spiral-shaped resonators	1.5-3	300
[68]	2019	H-shaped metamaterial	2.65	530
[69]	2019	Tamm plasmon-polaritons	1.132	700
[70]	2020	Split ring resonator metamaterial	0.1-1.9	300
[71]	2020	Ring resonator metamaterial	0.4-2.5	500
[72]	2021	Graphene split ring-resonator	1.4	453
[73]	2021	Graphene plasmonic meta surface	14	745
This work	2021	Folded Split-Ring Metamaterial Graphene Resonators	2-6	851

5. Conclusion

In summary, a graphene-based metamaterial (MTM) perfect absorber (MPA) in THz band for biosensor application is proposed. The structure is based on folded split-ring resonators. The structure is simulated using the finite element method and the obtained results show that when the chemical potential of graphene is $\mu_c=0.5$ eV, the proposed design has the best performance. The sensor has near perfect absorption with a spectral absorption coefficient of 99.75% at frequency 4 THz. Due to the high sensitivity and high FOM of the designed system, it can be used as a high performance refractive index (RI) biosensor. The findings indicate that the plasmonic sensor can achieve an average absorption value of 0.987 and a Q -factor of 13.76, a sensitivity of 851 GHz/RIU (corresponding to 15.59 $\mu\text{m}/\text{RIU}$).

Authors' declarations

- > Funding: This research received no funding.
- > Conflicts of interest/Competing interests: The authors have no relevant financial or non-financial interests to disclose.
- > Availability of data and materials: The datasets generated and analyzed during the current study are available from the corresponding author on reasonable request.
- > Code availability: Not applicable

- > Authors' contributions: Design, analysis and investigation: Mohammad-Reza Nickpay; Writing - original draft preparation: Mohammad-Reza Nickpay; Writing - review and editing: Mohammad Danaie; Supervision Mohammad Danaie and Ali Shahzadi.
- > Ethical Approval: We the undersigned declare that the manuscript entitled " Highly Sensitive THz Refractive Index Sensor Based on Folded Split-Ring Metamaterial Graphene Resonators" is original, has not been fully or partly published before, and is not currently being considered for publication elsewhere. Also, results are presented clearly, honestly, and without fabrication, falsification or inappropriate data manipulation. We confirm that the manuscript has been read and approved by all named authors and that there are no other persons who satisfied the criteria for authorship but are not listed. We further confirm that the order of authors listed in the manuscript has been approved by all of us.
- > Consent to Participate: Not applicable
- > Consent for publication: Not applicable

References

- [1] Nickpay, M.R., Danaie, M. and Shahzadi, A., 2020. A Wideband and Polarization-Insensitive Graphene-Based Metamaterial Absorber. *Superlattices and Microstructures*, p.106786.
- [2] Nickpay, M.R., Danaie, M. and Shahzadi, A., Design of a multi-band metamaterial perfect graphene-based absorber in THz frequency range for refractive index sensor. (in press)
- [3] Zhang XW, Qi YP, Zhou PY, Gong HH, Hu BB, Yan CM. Refractive index sensor based on fano resonances in plasmonic waveguide with dual side-coupled ring resonators. *Photon Sens* 2018;8:367–74.
- [4] Cen C, Lin H, Huang J, Liang C, Chen X, Tang Y, et al. A tunable plasmonic refractive index sensor with nanoring-strip graphene arrays. *Sensors* 2018;18:4489.
- [5] Wang XX, Wu XX, Zhu JK, Pang ZY, Yang H, Qi YP. Theoretical investigation of a highly sensitive refractive-index sensor based on TM0 waveguide mode resonance excited in an asymmetric metal-cladding dielectric waveguide structure. *Sensors* 2019;19:1187.
- [6] Wang B, Zhai X, Wang G, Huang W, Wang L. A novel dual-band terahertz metamaterial absorber for a sensor application. *J Appl Phys* 2015;117:014504.
- [7] Wang B, Wang G, Sang T. Simple design of novel triple-band terahertz metamaterial absorber for sensing application. *J Phys D Appl Phys* 2016;49:165307.
- [8] Xu, W., Xie, L. and Ying, Y., 2017. Mechanisms and applications of terahertz metamaterial sensing: a review. *Nanoscale*, 9(37), pp.13864-13878.
- [9] Valentine, J., Zhang, S., Zentgraf, T., Ulin-Avila, E., Genov, D.A., Bartal, G. and Zhang, X., 2008. Three-dimensional optical metamaterial with a negative refractive index. *nature*, 455(7211), pp.376-379.
- [10] Pendry, B.J., 2006. Metamaterials and negative refraction. *Nature Materials*, 5, pp.755-64.
- [11] Luo, X., Zhai, X., Wang, L. and Lin, Q., 2018. Enhanced dual-band absorption of molybdenum disulfide using a plasmonic perfect absorber. *Optics express*, 26(9), pp.11658-11666.
- [12] Jylhä, L., Kolmakov, I., Maslovski, S. and Tretyakov, S., 2006. Modeling of isotropic backward-wave materials composed of resonance spheres. *Journal of Applied Physics*, 99(4), p.043102.
- [13] Wang B, Zhai X, Wang G, Huang W, Wang L. A novel dual-band terahertz metamaterial absorber for a sensor application. *J Appl Phys* 2015;117:014504.
- [14] Wang B, Wang G, Sang T. Simple design of novel triple-band terahertz metamaterial absorber for sensing application. *J Phys D Appl Phys* 2016;49:165307.
- [15] Zeng Y, Chen XF, Yi Z, Yi YG, Xu XB. Fabrication of p-n heterostructure ZnO/Si moth-eye structures: antireflection, enhanced charge separation and photocatalytic properties. *Appl Surf Sci* 2018;441:40–8.
- [16] Yan YX, Yang H, Yi Z, Li RS, Wang XX. Enhanced photocatalytic performance and mechanism of Au@CaTiO₃ composites with Au nanoparticles assembled on CaTiO₃ nanocuboids. *Micromachines* 2019; 10:254.
- [17] Di LJ, Yang H, Xian T, Liu XQ, Chen XJ. Photocatalytic and photo-Fenton catalytic degradation activities of Z-scheme Ag₂S/BiFeO₃ heterojunction composites under visible-light irradiation. *Nanomaterials* 2019;9:399.
- [18] Liu G, Chen J, Pan P, Liu Z. Hybrid metal-semiconductor meta-surface based photoelectronic perfect absorber. *IEEE J Sel Top Quantum Electron* 2019;25:1–7.
- [19] Sarisaman M, Tas M. PT-symmetric coherent perfect absorber with grapheme. *J Opt Soc Am B* 2018;35:2423–32.

- [20] Gao HJ, Wang F, Wang SF, Wang XX, Yi Z, Yang H. Photocatalytic activity tuning in a novel Ag₂S/CQDs/CuBi₂O₄ composite: synthesis and photocatalytic mechanism. *Mater Res Bull* 2019;115:140–9.
- [21] Zhao XX, Yang H, Li SH, Cui ZM, Zhang CR. Synthesis and theoretical study of largesized Bi₄Ti₃O₁₂ square nanosheets with high photocatalytic activity. *Mater Res Bull* 2018;107:180–8.
- [22] Yan YX, Yang H, Zhao XX, Li RS, Wang XX. Enhanced photocatalytic activity of surface disorder-engineered CaTiO₃. *Mater Res Bull* 2018;105:286–90.
- [23] Nasirifar, R., Danaie, M. and Dideban, A., 2019. Dual channel optical fiber refractive index sensor based on surface plasmon resonance. *Optik*, 186, pp.194-204.
- [24] Rahmatiyar, M., Danaie, M. and Afsahi, M., 2020. Employment of cascaded coupled resonators for resolution enhancement in plasmonic refractive index sensors. *Optical and Quantum Electronics*, 52(3), pp.1-19
- [25] Rahman-Zadeh, F., Danaie, M. and Kaatuzian, H., 2019. Design of a highly sensitive photonic crystal refractive index sensor incorporating ring-shaped GaAs cavity. *Opto-Electronics Review*, 27(4), pp.369-377.
- [26] Rahmatiyar, M., Afsahi, M. and Danaie, M., 2020. Design of a refractive index plasmonic sensor based on a ring resonator coupled to a MIM waveguide containing tapered defects. *Plasmonics*, 15(6), pp.2169-2176.
- [27] Armaghani, S., Khani, S. and Danaie, M., 2019. Design of all-optical graphene switches based on a Mach-Zehnder interferometer employing optical Kerr effect. *Superlattices and Microstructures*, 135, p.106244.
- [28] Yi, Z., Huang, J., Cen, C., Chen, X., Zhou, Z., Tang, Y., Wang, B., Yi, Y., Wang, J. and Wu, P., 2019. Nanoribbon-ring cross perfect metamaterial graphene multi-band absorber in THz range and the sensing application. *Results in Physics*, 14, p.102367.
- [29] Huang J, Niu G, Yi Z, Chen XF, Zhou ZG, Ye X, et al. High sensitivity refractive index sensing with good angle and polarization tolerance using elliptical nanodisk grapheme metamaterials. *Phys Scr* 2019. <https://doi.org/10.1088/1402-4896/ab185f>.
- [30] Wang XX, Bai XL, Pang ZY, Zhu JK, Wu Y, Yang H, et al. Surface-enhanced Raman scattering by composite structure of gold nanocube-PMMA-gold film. *Opt Mater Express* 2019;9:1872–81.
- [31] Chen XF, Cen CL, Zhou L, Cao RF, Yi Z, Tang YJ. Magnetic properties and reverse magnetization process of anisotropic nanocomposite permanent magnet. *J Magn Magn Mater* 2019;483:152–7.
- [32] Zhang QB, Liao J, Liao M, Dai JY, Ge HL, Duan T, et al. One-dimensional Fe7S8@C nanorods as anode materials for high-rate and long-life lithium-ion batteries. *Appl Surf Sci* 2019;473:799–806.
- [33] Li, D., Lin, S., Hu, F., Chen, Z., Zhang, W. and Han, J., 2019. Metamaterial Terahertz Sensor for Measuring Thermal-Induced Denaturation Temperature of Insulin. *IEEE Sensors Journal*, 20(4), pp.1821-1828.
- [34] Saadeldin, A.S., Hameed, M.F.O., Elkaramany, E.M. and Obayya, S.S., 2019. Highly sensitive terahertz metamaterial sensor. *IEEE Sensors Journal*, 19(18), pp.7993-7999.
- [35] Zhang, W., Lan, F., Xuan, J., Mazumder, P., Aghajani, M., Yang, Z. and Men, L., 2017, September. Ultrasensitive dual-band terahertz sensing with metamaterial perfect absorber. In 2017 IEEE MTT-S International Microwave Workshop Series on Advanced Materials and Processes for RF and THz Applications (IMWS-AMP) (pp. 1-3). IEEE.
- [36] Nickpay, M.R., Danaie, M. and Shahzadi, A., 2019. Wideband Rectangular Double-Ring Nanoribbon Graphene-Based Antenna for Terahertz Communications. *IETE Journal of Research*, pp.1-10.
- [37] Khani, S., Danaie, M. and Rezaei, P., 2019. Size reduction of MIM surface plasmon based optical bandpass filters by the introduction of arrays of silver nano-rods. *Physica E: Low-dimensional Systems and Nanostructures*, 113, pp.25-34.
- [38] Khani, S., Danaie, M. and Rezaei, P., 2019. Tunable single-mode bandpass filter based on metal-insulator-metal plasmonic coupled U-shaped cavities. *IET Optoelectronics*, 13(4), pp.161-171.
- [39] Danaie, M. and Geravand, A., 2018. Design of low-cross-talk metal-insulator-metal plasmonic waveguide intersections based on proposed cross-shaped resonators. *Journal of Nanophotonics*, 12(4), p.046009.
- [40] Hajshahvaladi, L., Kaatuzian, H. and Danaie, M., 2019. Design and analysis of a plasmonic demultiplexer based on band-stop filters using double-nanodisk-shaped resonators. *Optical and Quantum Electronics*, 51(12), p.391.
- [41] Khani, S., Danaie, M. and Rezaei, P., 2020. Realization of a plasmonic optical switch using improved nano-disk resonators with Kerr-type nonlinearity: A theoretical and numerical study on challenges and solutions. *Optics Communications*, 477, p.126359.
- [42] Shafagh, S.G., Kaatuzian, H. and Danaie, M., 2020. Analysis, design and simulation of MIM plasmonic filters with different geometries for technical parameters improvement. *Communications in Theoretical Physics*, 72(8), p.085502.
- [43] Liu X, Liu G, Tang P, Fu G, Du G, Chen Q, et al. Quantitatively optical and electrical adjusting high-performance switch by graphene plasmonic perfect absorbers. *Carbon* 2018;140:362–7.
- [44] Wang J, Yang L, Hu Z, He W, Zheng G. Analysis of graphene-based multilayer comblike absorption system based on multiple waveguide theory. *IEEE Photon Technol Lett* 2019;31:561–4.
- [45] Liu C, Yang L, Liu Q, Wang FM, Sun ZJ, Sun T, et al. Analysis of a surface plasmon resonance probe based on photonic crystal fibers for low refractive index detection. *Plasmonics* 2018;13:779–84.
- [46] Hanson, G.W., 2008. Dyadic Green's functions and guided surface waves for a surface conductivity model of graphene. *Journal of Applied Physics*, 103(6), p.064302.

- [47] Nejat, M. and Nozhat, N., 2020. Sensing and switching capabilities of a graphene-based perfect dual-band metamaterial absorber with analytical methods. *JOSA B*, 37(5), pp.1359-1366.
- [48] Cen, C., Yi, Z., Zhang, G., Zhang, Y., Liang, C., Chen, X., Tang, Y., Ye, X., Yi, Y., Wang, J. and Hua, J., 2019. Theoretical design of a triple-band perfect metamaterial absorber in the THz frequency range. *Results in Physics*, 14, p.102463.
- [49] Chen J, Zha TQ, Zhang T, Tang CJ, Yu Y, Liu YJ, et al. Enhanced magnetic fields at optical frequency by diffraction coupling of magnetic resonances in lifted metamaterials. *J Lightwave Technol* 2017;35:71.
- [50] Li CC, Xie BS, Chen J, He ZX, Chen ZS, Long Y. Emerging mineral-coupled composite phase change materials for thermal energy storage. *Energy Convers Manage* 2019;183:633–44.
- [51] Sánchez Pastor, Jesús, 2017. Sensitivity Analysis of Single Split Ring Resonators and Single Complementary Split Ring Resonators coupled to Planar Transmission Lines. Degree in Technology Engineering and Telecommunication Services - Graduate in Technology Engineering and Telecommunication Services. Polytechnic University of Valencia. Valencia.
- [52] Liu G, Liu X, Chen J, Li Y, Shi L, Fu G, et al. Near-unity, full-spectrum, nanoscale solar absorbers and near-perfect blackbody emitters. *Sol Energy Mater Sol Cells* 2019;190:20–9.
- [53] Liu G, Chen J, Pan P, Liu Z. Hybrid Metal-semiconductor meta-surface based photoelectronic perfect absorber. *IEEE J Sel Top Quant Electron* 2019;25(3):1–7.
- [54] Ma X, Xie M, Wu WQ, Zeng B, Wang Y, Wu XX. The novel fractional discrete multivariate grey system model and its applications. *Appl Math Model* 2019;70:402–24.
- [55] Ma, A., Zhong, R., Wu, Z., Wang, Y., Yang, L., Liang, Z., Fang, Z. and Liu, S., 2020. Ultrasensitive THz Sensor Based on Centrosymmetric F-Shaped Metamaterial Resonators. *FRONTIERS IN PHYSICS*, 8.
- [56] Nejad, H.E., Mir, A. and Farmani, A., 2019. Supersensitive and tunable nano-biosensor for cancer detection. *IEEE Sensors Journal*, 19(13), pp.4874-4881.
- [57] Mendis, R., Astley, V., Liu, J. and Mittleman, D.M., 2009. Terahertz microfluidic sensor based on a parallel-plate waveguide resonance cavity. *Applied Physics Letters*, 95(17), p.171113.
- [58] Astley, V., Reichel, K.S., Jones, J., Mendis, R. and Mittleman, D.M., 2012. Terahertz multichannel microfluidic sensor based on parallel-plate waveguide resonance cavities. *Applied Physics Letters*, 100(23), p.231108.
- [59] You, B., Lu, J.Y., Liu, T.A. and Peng, J.L., 2013. Hybrid terahertz plasmonic waveguide for sensing applications. *Optics express*, 21(18), pp.21087-21096.
- [60] Cong, L. and Singh, R., 2014. Sensing with THz metamaterial absorbers. *arXiv preprint arXiv:1408.3711*.
- [61] Fan, F., Chen, S., Wang, X.H., Wu, P.F. and Chang, S.J., 2014. Terahertz refractive index sensing based on photonic column array. *IEEE Photonics Technology Letters*, 27(5), pp.478-481.
- [62] Li, X., Song, J. and Zhang, J.X., 2016. Design of terahertz metal-dielectric-metal waveguide with microfluidic sensing stub. *Optics Communications*, 361, pp.130-137.
- [63] Soltani, A., Neshasteh, H., Mataji-Kojouri, A., Born, N., Castro-Camus, E., Shahabadi, M. and Koch, M., 2016. Highly sensitive terahertz dielectric sensor for small-volume liquid samples. *Applied Physics Letters*, 108(19), p.191105.
- [64] Keshavarz, A. and Vafapour, Z., 2019. Sensing avian influenza viruses using terahertz metamaterial reflector. *IEEE Sensors Journal*, 19(13), pp.5161-5166.
- [65] Vanani, F.G., Fardoust, A. and Safian, R., 2018. Design of double ring label-free terahertz sensor. *IEEE Sensors Journal*, 19(4), pp.1293-1298.
- [66] Chen, C.Y., Yang, Y.H. and Yen, T.J., 2013. Unveiling the electromagnetic responses of fourfold symmetric metamaterials and their terahertz sensing capability. *Applied Physics Express*, 6(2), p.022002.
- [67] Tang, P.R., Li, J., Du, L.H., Liu, Q., Peng, Q.X., Zhao, J.H., Zhu, B., Li, Z.R. and Zhu, L.G., 2018. Ultrasensitive specific terahertz sensor based on tunable plasmon induced transparency of a graphene micro-ribbon array structure. *Optics express*, 26(23), pp.30655-30666.
- [68] Hu, S., Liu, D., Yang, H., Wang, H. and Wang, Y., 2019. Staggered H-shaped metamaterial based on electromagnetically induced transparency effect and its refractive index sensing performance. *Optics Communications*, 450, pp.202-207.
- [69] Keshavarz, M.M. and Alighanbari, A., 2019. Terahertz refractive index sensor based on Tamm plasmon-polaritons with graphene. *Applied optics*, 58(13), pp.3604-3612.
- [70] Chen, T., Zhang, D., Huang, F., Li, Z. and Hu, F., 2020. Design of a terahertz metamaterial sensor based on split ring resonator nested square ring resonator. *Materials Research Express*, 7(9), p.095802.
- [71] Wang, Y., Zhu, D., Cui, Z., Yue, L., Zhang, X., Hou, L., Zhang, K. and Hu, H., 2020. Properties and Sensing Performance of All-Dielectric Metasurface THz Absorbers. *IEEE Transactions on Terahertz Science and Technology*, 10(6), pp.599-605.
- [72] Emaminejad, H., Mir, A. and Farmani, A., 2021. Design and Simulation of a Novel Tunable Terahertz Biosensor Based on Metamaterials for Simultaneous Monitoring of Blood and Urine Components. *Plasmonics*, pp.1-12.
- [73] Hamouleh-Alipour, A., Mir, A. and Farmani, A., 2021. Analytical modeling and design of a Graphene metasurface sensor for thermo-optical detection of terahertz plasmons. *IEEE Sensors Journal*.